Chapter 10
FFAG, Scaling

Abstract This Chapter is an introduction to Fixed-Field Alternating Gradient (FFAG) cyclic accelerators, and to the theoretical material needed for the simulation exercises. It relies on charged particle optics and acceleration concepts introduced in the previous cyclotron and synchrotron Chapters. It further addresses specific aspects, including
- scaling FFAG design,
- beam dynamics in radial sector and spiral sector FFAG rings,
- synchrotron acceleration,
- other acceleration techniques such as multiple bunch acceleration, serpentine acceleration, bucket acceleration.
Simulations use optical elements already met in the previous: TOSCA, CAVITE, i/o keywords such as FAISCEAU, FAISTORE, the SYSTEM command. They further develop on the modeling of strong index sector dipoles, edge focusing in a radial or spiral sector magnet, and simulation of these types of optics using FFAG and FFAG-SPI optical elements. In that sense they prepare to strong focusing optics simulations in the next Chapters.

Notations used in the Text

A	sector angle of a dipole
B; B_0	magnetic field at radius R; field value at reference radius R_0
$B_{\mathrm{x,y,s}}$	components of **B** in Serret-Frénet moving frame
$B\rho$; $B\rho_0$	particle rigidity: $B\rho = p/q$; for reference momentum p_0
C; C_0	closed orbit length: $C = \oint ds = 2\pi\mathcal{R}$; for reference momentum p_0
ds	increment in path length: $ds = \mathcal{R}d\vartheta = Rd\theta/\cos\phi$
E; E_{xtr}; E_{inj}; E_s	particle energy: E = $\gamma \mathrm{m_0 c^2}$; extraction; injection; synchronous
EFB	effective field boundary
f; $\mathcal{F}(\theta)$, $\mathcal{F}(r,\theta)$	flutter; field form, or flutter, factor
f_{rf}	acceleration frequency
h	RF harmonic number
I_1	fringe field integral
k	geometrical, or scaling, field index: $k = \frac{R}{B}\frac{\partial B}{\partial R} \approx -n\frac{R}{\rho}$
$\mathcal{L}$	magnetic length
m_0; m; M	particle rest mass; mass; mass in $\mathrm{eV/c^2}$ units
N	number of cells in a ring
n	radial field index in Serret-Frénet frame: $n = -\frac{\rho}{B}\frac{\partial B}{\partial x}$
pf	packing factor: $pf = \mathcal{L}/C$
p; p_0; δp, Δp	particle momentum; reference momentum; offset
q	particle charge
R; R_0	radial coordinate, from center of ring; reference
$\mathcal{R}$	average closed orbit radius: $\mathcal{R} = C\,/\,2\pi$
v	particle velocity
V_{rf}; $\hat{V}_{\mathrm{rf}}$	acceleration voltage; peak value
x, x', y, y', δl, $\delta p/p$	particle coordinates in the moving frame

Greek symbols

$\beta = v/c$; β_0; β_s	normalized velocity; reference; synchronous
β_u, α_u, γ_u; η_u	optical functions (u = x, y, l); dispersion
γ	Lorentz factor: $\gamma = E/m_0c^2 = E[eV]/M$
δ	relative momentum offset: $\delta = \delta p/p$
ϵ_u/π	Courant-Snyder invariant: $\gamma_{\mathrm{u}}\mathrm{u}^2 + 2\alpha_{\mathrm{u}}\mathrm{u}\mathrm{u}' + \beta_{\mathrm{u}}\mathrm{u}'^2 = \epsilon_{\mathrm{u}}/\pi$
$\epsilon_{\mathrm{u,rms}}$	beam emittance
ζ	spiral angle of a spiral sector dipole EFB
η	phase-slip factor
θ; ϑ	azimuthal coordinate; generalized azimutahl coordinate
κ	gap shape index
λ	fringe field extent
ω_{rf}	acceleration voltage angular frequency: $\omega_{\mathrm{rf}} = 2\pi f_{\mathrm{rf}}$
ρ	local curvature radius
ϕ	scalloping angle
ϕ_s	synchronous RF phase

symbols

$(*)'$, $\overline{(*)}$	$\frac{d(*)}{ds}$; $\frac{\int (*) ds}{\int ds}$, wherein $ds = (dR^2 + R^2 d\theta^2 + dy^2)^{1/2}$

Introduction

Fixed field alternating gradient (FFAG) accelerators came on the scene in the early 1950's [1, 2, 3]. Electrostatic accelerators, cyclotrons, betatrons and synchrotrons were part of the landscape at that time, as instruments for nuclear physics research, medical and industrial applications, X-ray generators, etc. Accelerators were on their way to high energies, with strong focusing, pulsed synchrotron cascades and collider rings taking over. The concept was explored as an alternate method to put strong focusing into action, liable to produce high intensity beams, and in particular high power proton beams, as a result of the large geometrical and momentum acceptance of the FFAG optics. Three electron models were built and operated in the 1953-1967 period, by the Midwestern Universities Research Association. FFAG studies produced a wealth of theoretical and computational contributions to beam theory and beam manipulation in cyclic accelerator magnets and RF systems.

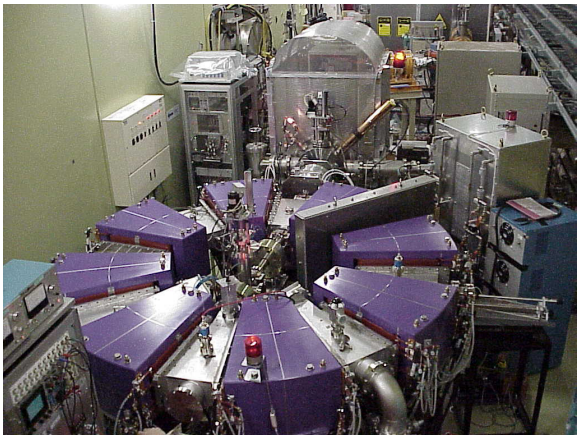

Fig. 10.1 PoP, the first proton FFAG, a 500 keV Proof-of-Principle 8-period ring operated at KEK from 1999 on. The 50 kV H^+ source can be seen in the background, and the injection line downstream which guides the beam through the ring vacuum chamber, onto the inner, injection orbit. Between two main dipole triplets to the right is a mgnetice alloy [29] accelerating cavity, and to the right its RF power system

Fig. 10.2 PoP defocusing-focusing-defocusing dipole triplet

Orbits spiral out in FFAGs, as a consequence of the fixed magnetic field, as in cyclotrons. On the other hand, by contrast with the latter, orbits at different

energies/different radii in FFAGs are non-isochronous: whereas the radial field index k is tailored to ensure isochronism in a cyclotron (k is R-rependent), it is constant in an FFAG to ensure zero-chromaticity, R-independent wave numbers, which has the side effect of confering them a large momentum acceptance. This adds to the large geometrical acceptance which results from their strong focusing optics. Due to their non-isochronous optics, FFAGs are normally (there are other ways, this is addressed in the following) operated as synchrocyclotrons, the acceleration is cycled: the accelerating voltage frequency is modulated from injection energy to top energy. Synchrocyclotron-like operation makes these machines prone to fast cycling, in the hundreds of kHz range with proper accelerating systems.

A revival of the field occurred in the late 1990s [4, 5, 6] (Fig. 10.1) leaning on progress on magnet and RF materials and technologies (Fig. 10.2), as well as improvements in beam dynamics simulation and magnet design software tools. This re-birth of FFAG R&D was driven by application of their fast-cycling and large geometrical and momentum acceptance properties, to high average intensity beam production and to the handling of short lived particle beams. Several proton and electron machines were built in Japan from the 1990s on [4], including an ADS prototype installation, internal target and beam cooling experiments [7, 8]. A prototype of a FFAG spiral sector dipole was built as part of a multiple-beam proton therapy facility design [10] (Fig. 10.3). Design studies over the years included high

Fig. 10.3 Prototype, full scale, and pole, of the spiral sector dipole of a 200 MeV proton therapy scaling FFAG design [10]

repetition rate, phase rotation, fast acceleration, with applications in cancer therapy, industrial irradiation, energy, production of neutrino beams (Fig. 10.4).

In summary, FFAG accelerator designs and techniques have been, and still are, investigated and experimented as a possible alternative to Linac, RCS or cyclotron, in

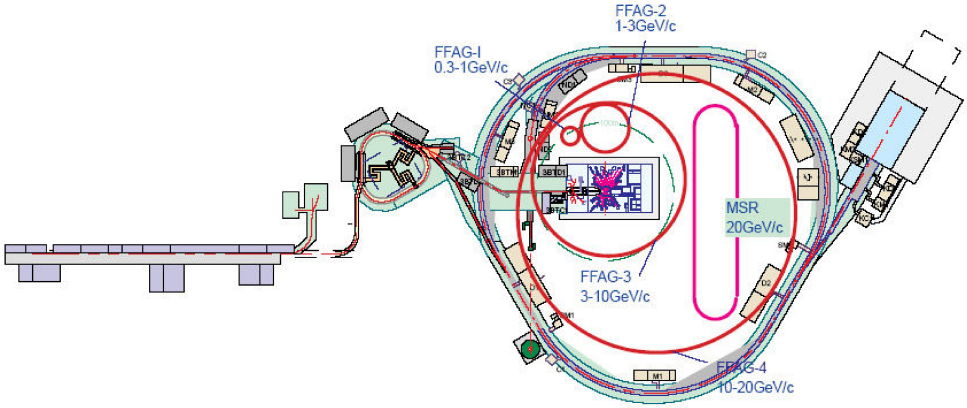

Fig. 10.4 Possible implementation of a scaling FFAG ring cascade for the acceleration of muons in a neutrino factory based on JPARC proton driver facility, from 0.3 GeV/c downstream of the production target to 20 GeV/c for injection in the muon decay ring (MSR) [**?**]

applications including proton drivers, proton therapy, fast acceleration of short-lived beams, etc.

10.1 Theory, Basic Concepts

Once a reference closed orbit is known, the Serret-Frénet coordinate system moving along that reference orbit around the FFAG ring is defined (Fig. 10.5). Linearized transverse particle motion across the magnetic elements, assuming a planar structure, satisfies Hill's equations

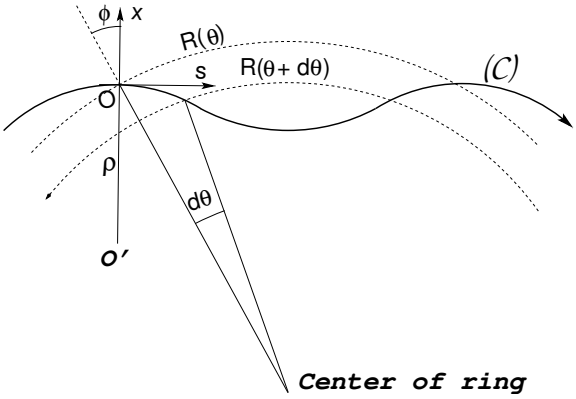

Fig. 10.5 Serret-Frénet frame $(O; s, x, y)$ tangent to the scalloping closed orbit in an FFAG ring. Particle position in the polar frame is $(R(\theta), \theta, y(\theta))$. Curvature at O is $1/\rho$, center of curvature is at O'. C is the closed orbit length (and defines an average radius $\mathcal{R} = C/2\pi$). ϕ is the scalloping angle [9]

$$\begin{cases} x'' + \dfrac{1-n}{\rho^2} x = 0 \\ y'' + \dfrac{n}{\rho^2} y = 0 \end{cases} \tag{10.1}$$

with s-dependent periodic coefficients $\frac{1-n}{\rho^2}$ and $\frac{n}{\rho^2}$. The radial index $n = -\frac{\rho}{B}\frac{\partial B}{\partial x}$ is a positive quantity in focusing sectors (ρ, B and $\partial B/\partial x$ all positive), negative in defocusing sectors (ρ, B and $\partial B/\partial x$ all negative) (Fig. 10.6).

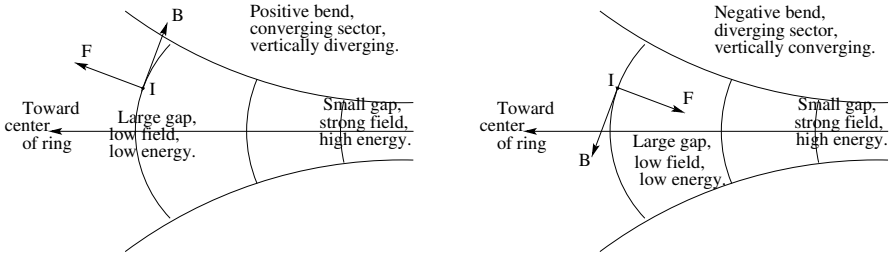

Fig. 10.6 Focusing and defocusing FFAG sectors

Scaling condition

Note that $\vartheta = s/\mathcal{R}$ and the polar angle θ as defined in Fig. 10.5 are related by $Rd\theta = \mathcal{R}\cos\phi\, d\vartheta$, with $\mathcal{R}$ the closed orbit length and ϕ the scalloping angle. In a simplified approach ignore the scalloping, namely,

$$\phi \approx 0, \quad \text{so that} \quad ds/d\vartheta \approx \mathcal{R} \quad \text{and} \quad d^2s/d\vartheta^2 \approx 0 \tag{10.2}$$

In this approximation, Eq. 10.1 yields

$$\begin{cases} \dfrac{d^2x}{d\vartheta^2} + \dfrac{R^2}{\rho^2}(1-n)x = 0 \\ \dfrac{d^2y}{d\vartheta^2} + \dfrac{R^2}{\rho^2} n y = 0 \end{cases} \tag{10.3}$$

At a given azimuth, $\vartheta \approx \theta$ in this simplified approach, constant radial and vertical focusing is equivalent to

$$\frac{d}{dp}\left((1-n)\frac{R^2}{\rho^2}\right)\bigg|_\theta = 0 \quad \text{and} \quad \frac{d}{dp}\left(n\frac{R^2}{\rho^2}\right)\bigg|_\theta = 0 \tag{10.4}$$

A sufficient condition for Eq. 10.4 is

$$\left.\frac{\partial}{\partial p}\left(\frac{R}{\rho}\right)\right|_{\theta=const} = 0 \qquad \text{and} \qquad \left.\frac{\partial n}{\partial p}\right|_{\theta=const} = 0 \tag{10.5}$$

Following the first condition, at a given azimuth the ratio of particle radial position to local curvature radius is constant, this is the geometrical similarity. Ignoring drift spaces between magnets, to the first order R can be identified with ρ, which results in geometrical similarity between orbits at different momenta. Following the second condition, at a given azimuth, particles with different momenta (thus different orbits) experience the same field index n ("zero-chromaticity" condition).

The geometrical similarity condition results in a constant geometrical field index

$$k = \frac{R}{B(R,\theta)} \left.\frac{\partial B(R,\theta)}{\partial R}\right|_R = -\frac{R}{\rho} n = constant \tag{10.6}$$

By integration, this yields the scaling field law

$$B(R) = B_0 \left(\frac{R}{R_0}\right)^k \tag{10.7}$$

Note in passing, given that $k = constant$, it results from Eq. 10.6 that a reversed sign dipole ($\rho < 0$) introduces a reversed-sign field index n, thus such alternating bend sign dipoles satisfy the FFAG concept of strong ($|n| \gg 1$) alternating gradient focusing. On the technology side: a way to obtain such radial field distribution is by shaping the dipole gap, with a gap height satisfying

$$g(R) \approx g_0 \left(\frac{R_0}{R}\right)^\kappa \qquad \text{with } \kappa \approx k \tag{10.8}$$

with greater (lower) gap at lower (greater) energy and radius (Fig. 10.6). Another way is by distributed current coils along the poles of a parallel gap dipole [12, 13]. Magnet design using 3D computer codes allows determining an accurate $g(R)$ shape, or proper current coil geometry and distribution, so to satisfy Eq. 10.7.

The momentum-dependent average orbit radius satisfies

$$\frac{R}{R_0} = \left(\frac{B\rho}{B\rho_0}\right)^{1/(k+1)} = \left(\frac{p}{p_0}\right)^{1/(k+1)} \tag{10.9}$$

In a general manner, in a lattice comprised of bends and field-free sections, the axial component of the magnetic field at location (R, θ) along an orbit in the median plane (y=0) satisfies

$$B(R,\theta) = B_0 \left(\frac{R}{R_0}\right)^k \mathcal{F}(\vartheta) \tag{10.10}$$

where the $2\pi/N$-periodic flutter factor $\mathcal{F}(\vartheta)$ describes the azimuthal variation of the field (the "gaps and valleys" of the AVF cyclotron, Chap. 4) in the $(\mathcal{R}, \vartheta)$ system. In the case of a radial sector FFAG the closed orbit scalloping is generally small (a few

percent of $\mathcal{R}$), ϑ can be considered to coincide with θ, and $\mathcal{F}(\vartheta)|_{\vartheta=\text{const.}}$ = constant (see Sec. 10.1.1). In a spiral sector FFAG, $\mathcal{F}(\vartheta)$ = constant determines a spiral curve, this is addressed in Sec. 10.1.2. A "flutter" can be computed and quantifies the departure of the azimuthal variation of the field from a step function ("hard-edge" model),

$$F = \frac{\overline{(\mathcal{F} - \overline{\mathcal{F}})^2}}{\overline{\mathcal{F}}^2} = \frac{\overline{(B - \overline{B})^2}}{\overline{B}^2} \xrightarrow{\text{hard-edge}} \frac{R}{\rho} - 1 \tag{10.11}$$

The R- and ρ-radius arcs share a common cord, which writes

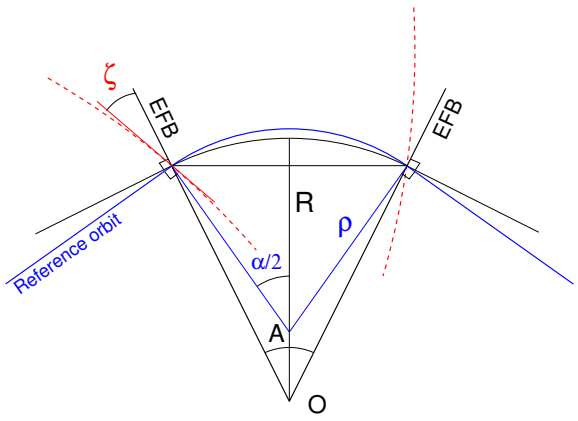

Fig. 10.7 Geometrical parameters of a radial sector FFAG dipole. O is the center of the ring and the EFBs form a sector angle A. The R-radius arc is a line of constant field (Eq. 10.7). The reference closed orbit, momentum $p = qB\rho$, subject to deviation α across the sector, is approximately on ρ-radius arc. Both arcs share the same cord (Eq. 10.12). The dashed lines figure the EFBs in the case of a spiral sector with spiral angle ζ

$$R \sin(A/2) = \rho \sin(\pi/N) \tag{10.12}$$

The packing factor takes the value

$$pf = \mathcal{L}/C = A/(2\pi/N) \tag{10.13}$$

Orbits

In a general manner, closed orbits need be computed numerically, searching for the momentum-dependent closed solution over a turn, or over a cell. They feature small amplitude scalloping in the vicinity of an average circular path with radius $R(p)$ (Eq. 10.9), thus initial conditions for numerical search can be taken as $R \approx R(p)$ and R' small.

The orbit excursion, from injection momentum to extraction momentum, satisfies (Eq. 10.9)

$$R_{xtr} - R_{inj} = R_0 \left(1 - \left(\frac{p_{inj}}{p_{xtr}}\right)^{\frac{1}{1+k}}\right) \tag{10.14}$$

The orbit length scales with momentum, following

$$C(p) = C_0 \left(\frac{p}{p_0} \right)^{\frac{1}{k+1}} \tag{10.15}$$

Focusing

There is two ways that the FFAG technique implements strong focusing,

- one consists in alternating strong transverse gradients (large $|n|$, see Eq. 10.6), which is achieved as pointed earlier by alternating normal-bend and reversed-bend magnets - however with the detrimental effect of decreased packing factor, increased circumference of the ring (more in Sec. 10.1.1),

- a second method relies on Thomas focusing, using spiral EFBs. A large spiral angle (strong vertical focusing, radially defocusing) compensates the large field index (strong radial focusing, vertically defocusing) (more in Sec. 10.1.2).

Wedge focusing

The strength of the focusing effect of a dipole edge satisfies, in the linear approach (Sec. 18.4.3)

$$f_{\mathrm{H}}^{-1} = \frac{\tan(\epsilon)}{\rho} \text{ (radial)} \quad \text{and} \quad f_{\mathrm{V}}^{-1} = -\frac{\tan(\epsilon - \psi)}{\rho} \text{ (vertical)} \tag{10.16}$$

with ϵ the wedge angle and ρ the local curvature radius. ψ is a correction to the wedge angle for the fringe field extent $\lambda \sim$ gap height, and writes

$$\psi = \frac{I_1 \, \lambda \, (1 + \sin^2(\epsilon))}{\rho \, \cos(\epsilon)} \quad \text{with} \quad I_1 = \int_{\text{edge}} \frac{B(s) \, (B_0 - B(s))}{\lambda \, B_0^2} \, ds \tag{10.17}$$

I_1 characterizing the effect of the fringe field shape. It may be assumed, considering dipole technologies of concern here, that I_1 does not depend on R [14]. Thus, given that $\rho \propto R$ (Eq. 10.12),

- constant horizontal wedge focusing is satisfied if ϵ is constant,

- constant vertical wedge focusing is satisfied if both ϵ and ψ are constant.

Equation 10.17 indicates that, in the case of constant wedge angle, $\psi =$ constant if $\lambda \propto r$, which requires that gap height to increase linearly with radius. In the gap shaping method (Eq. 10.8) the gap decreases with radius instead (Figs. 10.2, 10.6), thus leading to an increase in vertical tune with energy, unless proper measures are taken to overcome that effect [14].

From Eq. 10.16, constant wedge focusing requires the focal length to be proportional to the local orbit radius, *i.e.* (Eq. 10.12) proportional to the orbit length $C = 2\pi\mathcal{R} \approx 2\pi R$. Constant wedge angle is achieved with a logarithmic spiral edge [2], this is further addressed in Sec. 10.1.2.

Approximate wave numbers

An approximation of the radial and axial tunes is

$$\nu_R \approx \sqrt{1+k}, \quad \nu_y \approx \sqrt{-k + F^2(1+2\tan^2\zeta)} \tag{10.18}$$

not necessarily very accurate yet helpful in evaluating the relative effects of a small change of value of the flutter F, of the geometrical field index k, or of the spiral angle ζ in addition in the case of a spiral sector.

10.1.1 Radial Sector

A radial sector scaling FFAG is shown in Fig. 10.8 [15]: a 150 MeV ring built and operated at KEK in the early 2000s. The ring periodicity is N=12, a cell is comprised

Fig. 10.8 A 150 MeV 12-cell scaling FFAG ring, and its cyclotron injector (left). Its lattice cell magnet: a DFD dipole triplet (right). The gap shape follows Eq. 10.8 so ensuring the scaling field law (Eq. 10.7) [15]

of a DFD dipole triplet and a drift. The radial dependence of the magnetic field in the D and F sectors satisfies Eq. 10.10, it results from a shaping of their gap following Eq. 10.8 (as in the prototype PoP dipole, Fig. 10.2). The main parameters are summarized in Table 10.1.

Hall-probe measurements of the dipole triplet magnetice field are displayed in Fig. 10.9. Simulation-wise, the longitudinal modulation of the field across the dipole triplet (along the X-axis of the measurement frame) as observed in Fig. 10.9 can be modeled using the $\mathcal{F}(\theta)$ flutter factor in Eq. 10.10.

These measurements are for an isolated triplet, however, mutual influence in the ring is at the origin of a constant field, 200 Gauss about, across the drift between two dipole triplets, this is apparent in Fig. 10.9 which shows the related OPERA simulation in the periodic hypothesis [16]. This will be subject to simulation in the exercises.

Table 10.1 Design parameters of the a radial sector 150 MeV proton scaling FFAG.

Injection - extraction energy	MeV	12 - 150
Injection - extraction radius	m	4.7 - 5.2
Lattice		DFD
Number of cells (N)		12
Maximum β_R; β_z max.	m	3.8; 1.3
Tunes, ν_R; ν_z		3.7; 1.2
Magnet		
Type		radial sector DFD triplet
Sector angle A_D; A_F	deg	3.43; 10.24
Injection - extraction gap height	cm	20 - 4
Scaling index $k_D = k_F$		7.6
B_D; B_F, at 150 MeV	T	-1.21745; 1.69056
Acceleration		
Frequency swing	MHz	1.5 - 4.6
Harmonic		1
Voltage, peak-to-peak	kV	19
Cycle time	ms	4
Maximum repetition rate	Hz	250
Equivalent dB/dt	T/s	280
Synchrotron tune ν_s		0.039 - 0.012

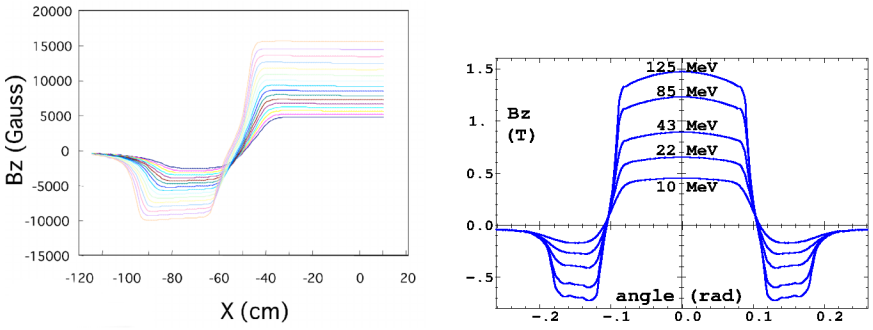

Fig. 10.9 Left: measured vertical magnetic field $B_Z(X)$, along R=constant arcs across one half of the radial sector dipole triplet [15]. The X coordinate is along an axis normal to the vertical symmetry plane of the triplet (the X=0 plane). The field on the plateau accurately follows the r^k scaling law (Eq.10.7), lower (greater) field at lower (greater) energy, greater (lower) dipole gap. Right: field along the periodic orbits across the cell at various energies (proton), from raytracing in an OPERA field map of the dipole triplet [16]

Transverse acceptance

Large dynamical transverse acceptance is an inherent property of scaling FFAG lattices. As an illustration of that property, the expected radial dynamical acceptance of Fig. 10.8 radial sector FFAG ring is displayed in Fig. 10.10. The latter has been obtained from raytracing in a theoretical field model built from Eqs. 10.10 and 10.33 as to the radial dependence of the field and accounting for Eq. 18.25 (Enge's field fall-off model) as to the flutter.

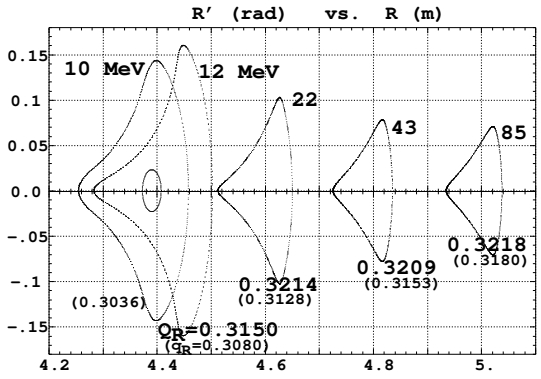

Fig. 10.10 Radial motion stability limit (at 10^3 turns) at various energies. The ellipse within the 10 MeV stability invariant on the left represents the nominal $\epsilon_R = 0.04\ \pi$cm beam at injection in the FFAG ring. The radial cell tune at stability limit (Q_R) and paraxial (q_R, between parentheses, almost energy-dependent) are given as an indication of the detuning resulting from the large amplitude of the motion [16]

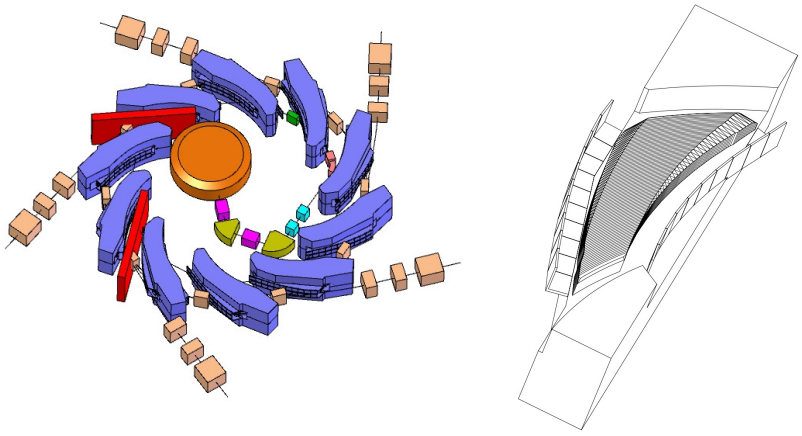

Fig. 10.11 Left: RACCAM proton therapy scaling FFAG ring design, and its variable energy H^- cyclotron injector. Right: a schema of its spiral dipole half-yoke, showing the gap shaping pole piece with its variable width chamfers and the EFB field clamps, two features that result in quasi-constant vertical tune [17]. In this prototype FFAG dipole the spiral EFB has a constant angle $\zeta = 53.7^o$ (Tab. 10.2)

10.1.2 Spiral Sector

A typical design of a spiral sector scaling FFAG is shown in Fig. 10.11: a variable energy and multiple extraction 230 MeV ring, aimed at cancer tumor treatment [17, 18]. Table 10.2 summarizes the parameters of the FFAG magnet and ring. The ring periodicity is N=10, a cell is comprised of a spiral sector dipole and a drift (geometrical parameters of the spiral sector are defined in Fig. 10.7). The radial dependence of the magnetic field in the spiral dipole satisfies Eq. 10.10 and results from the gap shape which follows Eq. 10.8. The RACCAM study included magnet prototyping and field

Table 10.2 Design parameters of the RACCAM proton therapy spiral sector scaling FFAG ring. Some of the parameter values vary with variable operation energy: values given here concern the extraction energy range 70 → 180 MeV

		Injection	Extraction
energy, variable	MeV	5.55 → 15	70 → 180
$B\rho$	T.m	0.341 → 0.562	1.231 → 2.030
$B\rho_{\text{extr.}}/B\rho_{\text{inj.}}$		3.612	
$\beta\gamma$		0.109 → 0.180	0.393 → 0.648
Lattice type		spiral, scaling	
Number of cells (N)		10	
Packing factor (pf)		0.34	
Drift length	m	1.15	1.42
Orbit radius (R)	m	2.794	3.460
Orbit excursion (Eq. 10.9)	m	0.667	
Tunes ν_R (constant); ν_y		2.76; 1.55 → 1.60	
Transition gamma (γ_{tr})		2.45	
Magnet			
Type		spiral sector	
Sector angle (A)	deg.	12.24	
Spiral angle (ζ)	deg.	53.7	
Scaling index k		5	

measurements which covered up to 2 T operation, corresponding to 230 MeV extraction energy [14, 19]. Hall-probe field measurements are displayed in Fig. 10.12. Magnetic field from OPERA field maps produced during the design of the magnet

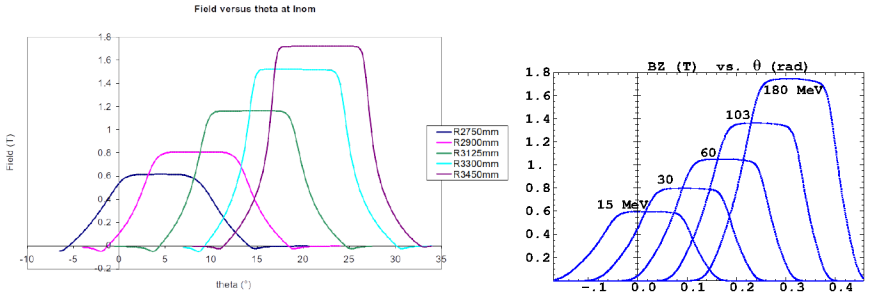

Fig. 10.12 Left: measured vertical magnetic field $B_Z(\theta)$, along R=constant arcs across RACCAM spiral sector dipole [19]. The field on the plateau accurately follows the R^k scaling law (Eq.10.7), lower (greater) field at lower (greater) energy, greater (lower) dipole gap. Right: field along the closed orbits across the dipole at various energies (proton), from raytracing in one of the many OPERA field maps produced during RACCAM spiral dipole design

are also given in Fig. 10.12.

Constant wedge angle

In the case of a ring lattice based on a single dipole (this includes separated sector cyclotrons) spiral EFBs with large spiral angle ζ (ζ is null in the case of a radial sector dipole) allows compensating the vertically defocusing effect of the field index (Eq. 10.18), whereas, as mentioned earlier, a spiral EFB has the merit of ensuring constant wedge angle and thus R-independent focusing. A spiral sector field boundary is defined by

$$\vartheta = \theta - \tan\zeta \, \ln\frac{R}{R_0} = \textit{constant}, \qquad \textit{i.e.}, \qquad R = R_0 \exp\left(\frac{\theta}{\tan\zeta}\right) \tag{10.19}$$

Note that an $\frac{R}{R_0}$-homothety, $\frac{2\pi}{N}$-rotation orbit similarity results, which reduces to a simple homothety in a radial lattice as $\zeta = 0$.

It follows from Eq. 10.19 that the median plane field at location (R, θ) in a spiral sector can be written under the form

$$B(R,\theta) = B_0 \left(\frac{R}{R_0}\right)^k \mathcal{F}\left(\tan\zeta \, \ln\frac{R}{R_0} - \theta\right) \tag{10.20}$$

wherein $\mathcal{F}\left(\tan\zeta \, \ln\frac{R}{R_0} - \theta\right)$ is a $\frac{2\pi}{N}$-periodic function of θ. A simple model for $\mathcal{F}(R,\theta)$, often used as a first approach in designing an N-periodic ring lattice, is a sinusoidal longitudinal modulation of the field of the form

$$\mathcal{F}(R,\theta) = 1 + f \, \sin\left(N\,(\tan\zeta \, \ln\frac{R}{R_0} - \theta)\right) \tag{10.21}$$

Numerical modeling

The parametric form of the equation of a spiral EFB is convenient for modeling the field. In proper (O;x,y) Cartesian frame, with geometrical parameters as recalled in Fig. 10.13, the parametric equations writes [18]

$$\begin{cases} x = e^{\theta/\tan\zeta} \, R_0 \cos(\omega + \theta) \\ y = e^{\theta/\tan\zeta} \, R_0 \sin(\omega + \theta) \end{cases} \tag{10.22}$$

with ω an angle which positions the EFB spiral in the (R, θ) frame. Fringe field computation following the method described in Sec. 18.5 then requires the distance

$$d(R,\theta) = ((x - X_M)^2 + (y - Y_M)^2)^{1/2} \tag{10.23}$$

from the projected particle position $(X_M(R,\theta), Y_M(R,\theta))$ to the projection of the latter on the spiral EFB. From the equation of the normal to the spiral it results that

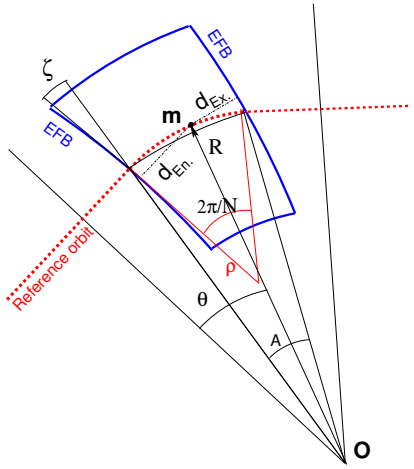

Fig. 10.13 Geometrical parameters used to computed the distance $d(R, \theta)$ from the projected particle position $m(R, \theta)$ in the median plane to the spiral sector EFBs (distances respectively $d_{\text{En.}}$ and $d_{\text{Ex.}}$)

$$\left(X_M - e^{\frac{\theta}{\tan\zeta}} R_0 \cos(\omega+\theta)\right)\left(\frac{e^{\frac{\theta}{\tan\zeta}}}{\tan\zeta} R_0 \cos(\omega+\theta) - e^{\frac{\theta}{\tan\zeta}} R_0 \sin(\omega+\theta)\right) \quad (10.24)$$
$$+\left(Y_M - e^{\frac{\theta}{\tan\zeta}} R_0 \sin(\omega+\theta)\right)\left(e^{\frac{\theta}{\tan\zeta}} R_0 \cos(\omega+\theta) + \frac{e^{\frac{\theta}{\tan\zeta}}}{\tan\zeta} R_0 \sin(\omega+\theta)\right) = 0$$

The value of θ is obtained by numerically solving this equation, which from Eq. 10.22 yields (x, y), and thus $d(R, \theta)$ (Eq. 10.23).

Note that nothing precludes introducing a dependence in R of the spiral angle, $\zeta(R)$ [18], as happens in cyclotrons where the focusing index k is tailored (changes with R) to ensure isochronism, requiring in turn ζ to change with R in order to maintain proper vertical focusing. This property was accounted for in the model used in defining the geometry of the magnet which resulted in the OPERA fields shown in Fig. 10.12. The resulting vertical tune proved to be essentially R-independent [14, 17].

Transverse acceptance

Spiral sector scaling FFAG lattices feature a large dynamical transverse acceptance. As an illustration of that property, the radial dynamical acceptance of RACCAM spiral sector FFAG ring (Fig. 10.11) is displayed in Fig. 10.14. The latter has been obtained from raytracing in a theoretical field model built from Eqs. 10.10 and 10.33 as to the radial dependence of the field, whereas the azimuthal dependence is modeled using Eq. 18.25 and Enge's style fall-off (Eq. 18.25).

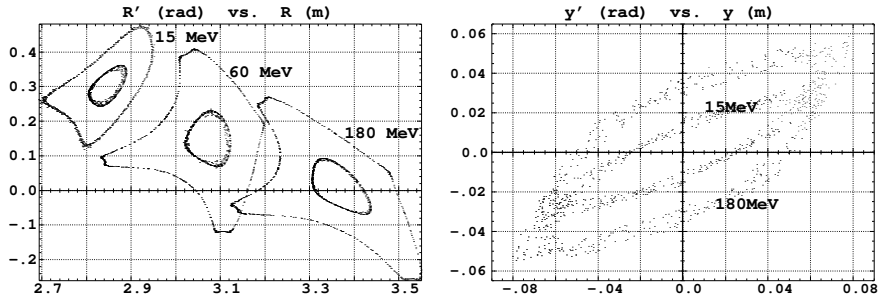

Fig. 10.14 Left: radial 1000-turn motion stability limits at various energies in RACCAM spiral sector ring design. The outer invariants are for pure radial motion, they are several $10^3\,\pi$mm mrad. The inner ones are the stability limit in the presence of small amplitude vertical motion, they are of the order of $10^3\,\pi$mm mrad, the reduction of the dynamical acceptance arises due to non-linear coupling. Right: vertical 1000-turn motion stability limits at 15 MeV (inner, elliptical shaped distribution) and 180 MeV (outer distribution), they are about $600\,\pi$mm mrad and $2000\,\pi$mm mrad, respectively

10.1.3 Longitudinal motion, acceleration

The revolution time around the ring $T_{rev} = C/\beta c$ can be written

$$T_{rev} = T_{rev,0}\left(\frac{p}{p_0}\right)^{\frac{1}{k+1}}\frac{\beta_0}{\beta} = T_{rev,0}\left(\frac{p}{p_0}\right)^{\frac{-k}{k+1}}\frac{E}{E_0} \tag{10.25}$$

with the index "0" denoting quantities which correspond to the reference momentum p_0. The RF phase on arrival of a particle at the RF gap at time t is

$$\phi(t) = 2\pi h\int_0^t f_{\mathrm{rf}}(t)dt$$

with $f_{\mathrm{rf}}(t)$ the revolution frequency law and h the harmonic number. $f_{\mathrm{rf}}(t)$ can be derived from the revolution time (Eq. 10.25), or more generally from the actual close orbit length (Eq. 10.15), including possible orbit bumps for instance.

The momentum compaction and transition γ stem from $p(R)$ (Eq. 10.9), namely

$$\alpha = \frac{\Delta C/C}{\Delta p/p} = \frac{1}{1+k} \quad \text{and} \quad \gamma_{tr} = \sqrt{1/\alpha} = \sqrt{1+k} \tag{10.26}$$

Synchronous acceleration in a scaling FFAG proceeds as in synchro-cyclotrons, longitudinal particle motion follows the principles of synchrotron phase stability (Chap. 7) [15, 17]. Momentum acceptance and synchrotron frequency write

$$\pm\frac{\Delta p}{p} = \pm\frac{1}{\beta_s}\left(\frac{2q\hat{V}_{\mathrm{rf}}}{\pi h\eta E_s}\right)^{1/2} \quad \text{and} \quad \nu_s = \frac{2\pi}{\beta_s}\left(\frac{h\eta\cos\phi_s\; q\hat{V}_{\mathrm{rf}}}{2\pi E_s}\right)^{1/2} \tag{10.27}$$

with the index "s" denoting quantities corresponding to the synchronous particle. A practical acceleration cycle may include single-bunch or multiturn injection, RF capture, synchronous acceleration, and single-turn kicker-septum extraction. Fixed-field allows fast acceleration and repetition rate up to hundreds of Hz with proper amount of accelerationg voltage, allowing for instance fast bunch-to-pixel tumor irradiation in the proton therapy application [17].

Other modes of acceleration have been studied and experimented, including

- multiple-bunch acceleration, by superposition of different frequency RF waves in the cavity [20],
- induction acceleration based on a betatron core [13],
- hybrid betatron-synchrotron acceleration [21, 22],
- bucket acceleration for fast acceleration of short lived muons [23],
- quasi-synchronous serpentine acceleration [24, 25],
- longitudinal phase rotation [26].

Betatron damping

In the presence of acceleration the equations of transverse motion write [31]

$$\begin{cases} x'' + \dfrac{(\gamma\beta)'}{(\gamma\beta)}x' + \dfrac{1-n}{\rho^2}x = 0 \\ y'' + \dfrac{(\gamma\beta)'}{(\gamma\beta)}y' + \dfrac{n}{\rho^2}y = 0 \end{cases} \tag{10.28}$$

(and $(\gamma\beta)' = 0$, absence of acceleration, yields Eq. 10.1). In the adiabatic approximation (slow damping, compared to betatron oscillation motion) the solutions can be written

$$\begin{matrix} x(s) \\ y(s) \end{matrix} = \frac{1}{\sqrt{|h_{\substack{x\\y}}|}} \frac{1}{\sqrt{\beta_b\gamma_b}} \left[A_{\substack{x\\y}} \exp\left(\int h_{\substack{x\\y}}\, ds \right) + B_{\substack{x\\y}} \exp\left(- \int h_{\substack{x\\y}}\, ds \right) \right] \tag{10.29}$$

with

$$\left.\begin{matrix} h_x^2(s) = -\dfrac{1-n}{\rho^2} \\ h_y^2(s) = -\dfrac{n}{\rho^2} \end{matrix}\right\} + \frac{1}{2}\frac{d}{ds}\left[\frac{(\gamma\beta)'}{(\gamma\beta)}\right] + \frac{1}{4}\left[\frac{(\gamma\beta)'}{(\gamma\beta)}\right]^2 \tag{10.30}$$

and $A_{\substack{x\\y}}$ and $B_{\substack{x\\y}}$ constants depending upon the initial conditions. Considering that $\rho \propto R$ (Eq. 10.6), assuming stable periodic motion, and dropping the $(\beta\gamma)'$ terms in Eq. 10.30 (h(s) slowly varying), it results from Eq. 10.29 that the transverse particle oscillations satisfy

$$x, y \propto \frac{\sqrt{R}}{\sqrt{\beta\gamma}}, \qquad x', y' \propto \frac{1}{\sqrt{R}\sqrt{\beta\gamma}} \tag{10.31}$$

thus the damping of betatron oscillations is R-dependent. An invariant ensemble average results,

$$\beta\gamma\, \epsilon_{rms} = \beta\gamma\, \left[< x^2 >< x'^2 > - < xx' >^2 \right]^{1/2} = \text{ constant} \tag{10.32}$$

i.e., betatron damping of the transverse emittances $\epsilon_{rms} \propto 1/\beta\gamma$.

10.2 Exercises

Preliminaries

1. Zgoubi users' guide at hand, when setting up the input data files to work out the exercises, is a must-have. PART B of the guide in particular, details the formatting of the input data lists following keywords (a few keywords only, for instance FAISCEAU, MARKER, YMY, do not require additional data), and gives the units to be used.
2. Regarding keywords: by "keyword" it is meant, the name of the optical elements, or I/O procedures, or commands, as they appear in a simulation input data file. Keywords are most of the time referred to without any additional explanation: it is understood that the users' guide is at hand, and details regarding the use and functioning to be sought there: in PART A of the guide, as to what a particular keyword does and how it does it; in PART B as to the formatting of the data list under a particular keyword. The users' guide INDEX is a convenient tool to navigate amongst keywords. A complete list may also be found in the "Glossary of Keywords", at the begining of both PART A and PART B of the users' guide, and an overview of what they can be used at is given in "Optical elements versus keywords".

   - The concise notation KEYWORDS[ARGUMENT1, ARGUMENT2, ...] used in the exercise: it follows the nomenclature of the Users' Guide, Part B. Consider a couple of examples:
     - OBJET[KOBJ=1] stands for keyword OBJET, and the value of KOBJ=1 retained here;
     - OPTIONS[CONSTY=ON] stands for keyword OPTIONS, and the option retained here, CONSTY, switched ON.
   - The keyword INCLUDE is used in many simulation input data files. The reason is mostly to reduce the length of these files (which would otherwise be prohibitively voluminous). Just as with the Latex, or Fortran, "include" command, a segment of an optical sequence subject to an INCLUDE may always be replaced by that very sequence segment.

3. Coordinate Systems: two sets of coordinate notations are used in the exercises,

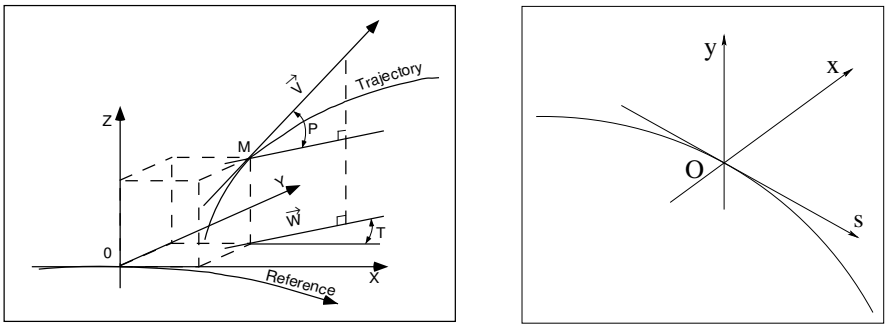

Fig. 10.15 Zgoubi Cartesian frame (O;X,Y,Z), and moving frame (O;s,x,y)

- on the one hand (and, in the Solutions Section mostly), zgoubi's (Y,T,Z,P,X,D) coordinates in the optical element reference frame (O;X,Y,Z), the very frame in which the optical element field $\mathbf{E}(X, Y, Z)$ and/or $\mathbf{B}(X, Y, Z)$ is defined (the origin for X depends on the optical element). Particle coordinates in this frame can be
  - either Cartesian, in which case X, Y (angle T) and Z (angle P) denote respectively the longitudinal, transverse horizontal and vertical coordinates,
  - or cylindrical, in which case, given m the projection of particle position M in the Z=0 plane, Y denotes the radius: $Y = |\mathbf{Om}|$, whereas X denotes the **OX**-**Om** angle (and, yes, the nature of the variables named X and Y in the source code does change);

  Note: the sixth zgoubi's coordinate above is

$$D = \frac{\text{particle rigidity}}{BORO}$$

  with BORO a reference rigidity, the very first numerical datum to appear in any zgoubi sequence, as part of the definition of initial particle coordinates by OBJET or MCOBJET. BORO may sometimes be denoted $B\rho_{\text{ref}}$, depending upon the context. Note that D-1 identifies with the above $\delta p/p$.
- on the other hand (and, in the exercise assignments mostly), the conventional (x,x',y,y',δl,$\delta p/p$) coordinates in the moving frame (O;s,x,y) or close variants.

Comments are introduced wherever deemed necessary (hopefully, often enough) in an effort to lift potential ambiguities regarding coordinate notations.

4. In the following exercises a superposition technique is used to simulate the field in a series of neighboring magnets. The method consists in computing the mid-plane field at any location (R, θ) by adding individual contributions, namely [27]

$$B_Z(R,\theta)|_{Z=0} = \sum_{i=1,N} B_{Z,i}(R,\theta)\big|_{Z=0} = \sum_{i=1,N} B_{0,i}\, \mathcal{F}_i(R,\theta)\, \mathcal{R}_i(R) \qquad (10.33)$$

with $\mathcal{F}_i(R,\theta)$ and $\mathcal{R}_i(R)$ in each individual dipole in the series (Eqs. 10.10, 10.20). Note that, in doing so it is not meant that field superposition would apply in reality (FFAG magnets are closely spaced, cross-talk may occurs), however it appears to allow closely reproducing magnet computation code outcomes.

10.2.1 A 150 MeV, Proton, Radial Sector FFAG

This series of exercises is based on the 150 MeV radial sector FFAG built and operated at KEK in the early 2000 (Fig. 10.8). The parameters of concern are given in Tab. 10.1 [15]. The cell geometry is sketched in Fig. 10.16. A simulation in zgoubi, an outcome of these exercises, is illustrated in Fig. 10.17.

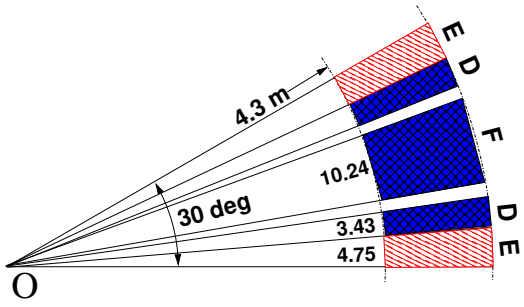

Fig. 10.16 Geometry of a 30 degree DFD cell. O is the center of the ring. F and D are respectively the focusing, 10.24 degree, and defocusing, 3.43 degree, sectors of the dipole triplet. The shadowed 4.75 degree "E" regions represent a half of the interval between two dipole triplets, a region of $\approx$ 200 G stray field [16, 27]

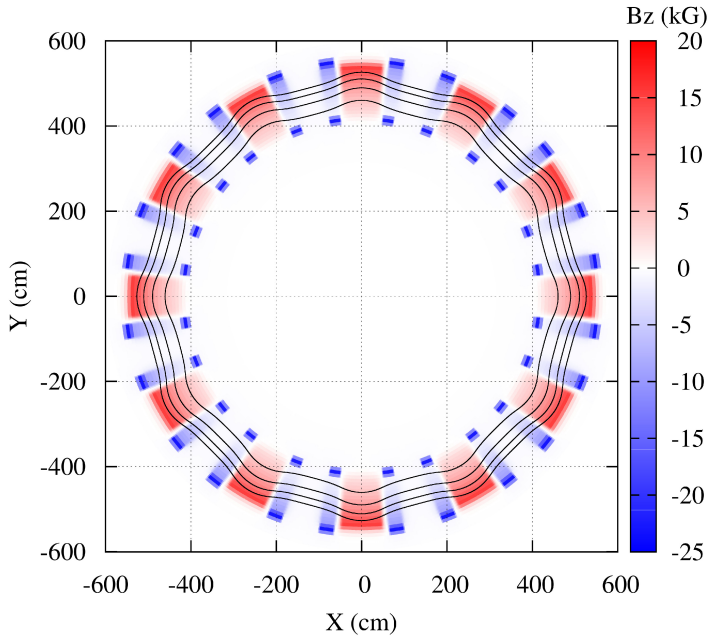

Fig. 10.17 A simulation of KEK 150 MeV FFAG ring in zgoubi, including a few orbits, using the keyword FFAG [31]. A graph obtained using gnuplot, geometrical data taken from zgoubi.dat, and particle data read from zgoubi.plt

10.1 Field in a Radial Sector Dipole Triplet

The FFAG keyword is based on Eqs. 10.10, 10.33 to generate the field from a magent N-tuple at particle location, while motion proceeds across the magnet. It includes for $\mathcal{F}_i(R,\theta)$ the fringe fall-off model described in Sec. 18.5. Using this keyword, produce a 3D view of the median plane field $B_Z(R,\theta)$ in the dipole triplet. The keyword OBJET[KOBJ=1] can be used to generate a proper trajectory sample, and OPTIONS[CONSTY=ON] to force them on constant radii. Option IL=2 under FFAG can be used to store step by log trajectory data in zgoubi.plt, and field data extracted from the latter for plotting.

10.2 Orbits, Scalloping

Characterizing the focusing properties of the lattice (say, over the radial span of the accelerated orbit) first requires finding the closed orbits over that radial extent. The radius - or momentum - dependence of optical functions may then be computed (exercise 10.4), as well as the radius dependence of the time of flight, a necessary ingredient to define the acceleration program (exercise 10.5), etc.

The input data file of exercise 10.1 can be used as a starting point, here.

(a) Compute a scan of the periodic orbits $R(\theta)$ across the cell, for a few proton energies ranging in $12 \le E \le 200$ MeV. REBELOTE can be used to loop on the energy (by changing the relative particle rigidity D under OBJET), preceded by FIT to find the periodic orbit at the energy of concern.

Plot these orbits $R(\theta)$, and on a separate graph the field $B(\theta)$ along the orbits. These data can be read from zgoubi.plt, using IL=2 under FFAG keyword.

(b) Show graphically the homothety of the orbits. Check the similarity ratio.

(c) By tracking, show that orbit excursion over an energy range $12 \le E \le 200$ MeV (average radius spans from R_{inj} to R_{xtr}), satisfies Eqs. 10.9, 10.14. Particle coordinates at some azimuth along the ring can be logged in that aim in zgoubi.res using FAISCEAU (a "grep" can grab them for plotting), or in an ancillary zgoubi.fai style file using FAISTORE.

(d) Evaluate the orbit "scalloping", *i.e.*, the maximum value of $|R(\theta) - R|/R$. Plot it as a function of energy.

10.3 Zero-Chromaticity

This exercise investigates the momentum dependence of the wave numbers.

(a) Compute and plot the momentum dependence of the radial and axial tunes in the 12-cell ring (Fig. 10.8). Use for that either one of the following two methods to obtain the tune values:

(a.1) From the cell transport matrix, using MATRIX. REBELOTE can be used in that case to repeat on momentum values.

(a.2) from Fourier analysis of small amplitude motion.

Compare the results with theory (Eq. 10.18).

(b) It can be observed that the radial tune is constant with momentum, or equivalently with the orbit radius R, this is expected from the scaling law (Eq. 10.7). However the axial tune is R-dependent. Explain why.

(c) In the field model, introduce a R-dependence of the gap of the form Eq. 10.8. Note: this is equivalent to introducing an R-dependence of the fringe field extent,

or equivalently of the field form factor $\mathcal{F}(\theta)$ in Eq. 10.10, proper to change the R-dependence of the axial focusing. Using an optimization (FIT) procedure, compute the value of κ which minimizes the change of ν_y over the energy interval $12 \leq E \leq 150$ MeV.

(d) Compute the value of the momentum compaction and transition γ_{tr} at two sample energies, 12 and 150 MeV. TWISS can be used for that, with OBJET[KOBJ=5]. Check their relationship to the radial tune.

10.4 Beam Envelopes; Phase Space

(a) Produce a graph of the trajectories of a beam bundle across the cell, at 12 and 150 MeV. Take initial coordinates evenly distributed on initial paraxial invariants. OBJET[KOBJ=8] can be used to define that set of particles.

(b) Perform single particle tracking, over many turns, using REBELOTE. Consider two cases, separately: paraxial motion, and large excursion motion. Show that large excursion phase space motion features non-linear coupling.

10.5 Acceleration: Transverse Betatron Damping

(a) Produce a simulation of the transverse and longitudinal motions of a particle taken on a small initial invariant, over a $10 \rightarrow 150$ MeV acceleration cycle in the 12-cell ring. Assume the following RF parameters: peak voltage $\hat{V} = 40$ kVolts, synchronous phase $\phi_s = 20^o$, harmonic h=1. Acceleration uses CAVITE[IOPT=6], which imposes defining the particle type, with PARTICUL; multiturn is obtained using REBELOTE. SCALING takes care of having magnetic fields ramped to follow momentum increase by CAVITE.

(b) Show graphically that the transverse betatron oscillation damping satisfies the R-dependence of Eq. 10.31.

(c) Accelerate a bunch of a few tens of particles. Check the beam emittance damping of Eq. 10.32.

10.2.2 RACCAM Proton Therapy Spiral Sector FFAG

This series of exercises is based on the 180 MeV spiral sector FFAG design of Fig. 10.11. The parameters of concern are given in Tab. 10.2 [14, 17, 18, 19]. The cell geometry is sketched in Fig. 10.18.

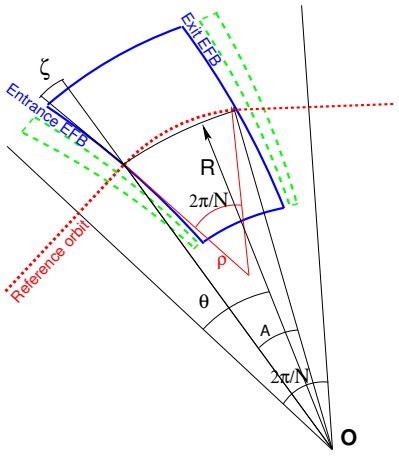

Fig. 10.18 A sketch of RACCAM spiral sector dipole and $2\pi/10$ cell. O is the center of the ring and the EFBs form a sector angle A. Note that the reference orbit is not strictly circular, the bending radius is not constant along the trajectory over the $2\pi/N$ arc (a line of constant field is an R-radius arc, centered on O).

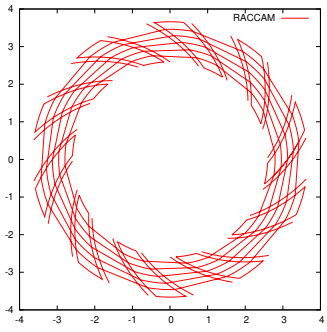

Fig. 10.19 A simulation of RACCAM FFAG ring in zgoubi, including a few orbits, using the keyword FFAG-SPI. A graph obtained using gnuplot, geometrical data taken from zgoubi.dat, and particle data read from zgoubi.plt

10.6 Field in a Spiral Sector Dipole

The FFAG-SPI keyword is based on Eq. 10.20 to generate the field from a spiral sector dipole (or several sectors side-by-side within an AT angular extent [30, Sec. FFAG-SPI]) at particle location, while motion proceeds across the magnet. It includes for $\mathcal{F}_i(R,\theta)$ the fringe fall-off model described in Sec. 18.5.

Using this keyword, produce a 3D view of the median plane field $B_Z(R,\theta)$ in the dipole. The keyword OBJET[KOBJ=1] can be used to generate a proper trajectory

sample, and OPTIONS[CONSTY=ON] to force them on constant radii. Option IL=2 under FFAG-SPI can be used to store step by log trajectory data in zgoubi.plt, and field data extracted from the latter for plotting.

Note that CYCLOTRON keyword could be used instead, if desired. It allows some sophistications regarding field modeling (and in the complexity of the exercises!) compared to using FFAG-SPI, such as accounting for an R-dependence of the geometrical field index k (Eq. 10.7) (a capability which is used in exercise 4.8, in the relativistic cyclotron Chapter, to adjust the isochronism), and of the fringe field extent, via the gap shape index κ (Eq. 10.8).

10.7 Orbits, Scalloping

Characterizing the focusing properties of the lattice (say, over the radial span of the accelerated orbit) first requires finding the periodic orbits over that radial extent. The radius - or momentum - dependence of optical functions may then be found (exercise 10.9), as well as the radius dependence of time of flight for further acceleration (exercise 10.14), etc.

(a) Compute a scan of the periodic orbits $R(\theta)$ across the cell, for a few proton energies ranging in $15 \leq E \leq 180$ MeV. REBELOTE can be used to loop on the energy (by changing the relative particle rigidity D under OBJET), preceded by FIT to find the periodic orbit at the energy of concern.

Plot these orbits $R(\theta)$, and on a separate graph the field $B(\theta)$ along the orbits. These data can be read from zgoubi.plt, using IL=2 under FFAG-SPI keyword.

(b) Show graphically the homothety-rotation of the orbits.

(c) By tracking, show that orbit excursion over an energy range $15 \leq E \leq 180$ MeV (average radius spans from R_{inj} to R_{xtr}), satisfies Eqs. 10.9, 10.14.

10.8 Zero-Chromaticity

(a) Compute and plot the momentum dependence of the radial and axial tunes in the 10-cell ring (Fig. 10.11). Use for that either one of the following two methods to obtain the tune values:

(a.1) from the cell transport matrix,

(a.2) from Fourier analysis of small amplitude motion.

Compare with expectations (Eq. 10.18).

(b) It can be observed that the radial tune is constant with momentum, or equivalently with the orbit radius R, this is expected from the scaling law (Eq. 10.7). However the axial tune is R-dependent. Explain why.

(c) In the field model, introduce a R-dependence of the gap of the form Eq. 10.8. Note: this is equivalent to introducing a R-dependence of the fringe field extent, or equivalently of the field form factor $\mathcal{F}(\theta)$ in Eq. 10.10, proper to change the R-dependence of the axial focusing. Using an optimization ("fitting") procedure, compute the value of κ which minimizes the change of ν_y over the energy interval $15 < E < 180$ MeV.

(d) Compute the value of the momentum compaction and transition γ_{tr}, at 12 and 150 MeV. Check their relationship to the radial tune.

10.9 Beam Envelopes, Optical Functions

Produce graphs of radial and vertical beam bundles across the cell, at 15 and 180 MeV. Derive from these the envelope values and the betatron function amplitudes.

10.10 Periodic Stability Domain

Vary the scaling index k and spiral angle ζ of the spiral dipole, in FFAG-SPI:

- produce a two-dimensional (ν_R, ν_y) tune scan diagram, covering the motion stability area resulting from varying k and ζ.

- produce the corresponding (k, ζ) stability limit diagram.

10.11 Motion Stability Limit

Tracking single particle radial motion in the OPERA field map of the FFAG dipole triplet, yields at stability limit the phase space portrait of Fig. 10.20 [16]. Re-produce a similar phase space graph at stability limit, using the analytical field model FFAG-SPI.

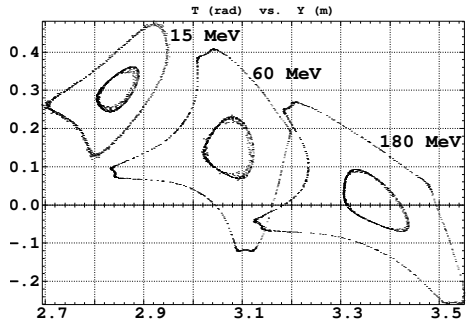

Fig. 10.20 Radial motion stability limits at three different energies, with either zero Z-motion (outer limits) or very small initial Z-motion (inner limits): non-linear coupling is responsible for the reduction of the dynamical acceptance

10.12 Dynamic Aperture

Extend the previous (exercise 10.11) stability limit search to produce the dynamic aperture in (Y,Z) space, at 15, 57 and 180 MeV.

10.13 Bucket height, Synchrotron Tune

Check momentum acceptance and synchrotron tune, Eq. 10.27

(a) in stationary bucket mode, at 15 and 180 MeV,

(b) in accelerating bucket mode.

10.14 Acceleration, Transverse Betatron Damping

Acceleration cycle in RACCAM ring.

Produce a simulation of a 15 $\rightarrow$ 180 MeV acceleration cycle in RACCAM ring, single particle. Take an acceleration rate of 10 kVolts per turn. Acceleration uses CAVITE[IOPT=6], which imposes defining the particle type, with PARTICUL; multiturn is obtained using REBELOTE. SCALING takes care of having magnetic fields ramped to follow momentum increase by CAVITE.

Show the betatron damping, graphically.

10.2.3 A 30 MeV Prototype Spiral Sector Doublet FFAG Ring

The ring considered here is a 30 MeV proton model of a high power 1.2 GeV proton FFAG [28]. Design parameters are given in Tab. 10.3. The 15-periodic ring is based on a 24^o degree cell comprised of a pair of spiral sector FFAG dipoles with opposite signs (Fig. 10.21), The "wrong sign" bend contributes increases the size of the ring; its purpose is to increase the flutter (Eq. 10.11), thus enhancing the axial focusing (Eq. 10.18), which in turn allows greater radial focusing (from greater scaling index k) for a given spiral angle. As a matter of fact it is desirable for the latter not to exceed $55 \sim 60$ degree, for magnet and ring construction purposes.

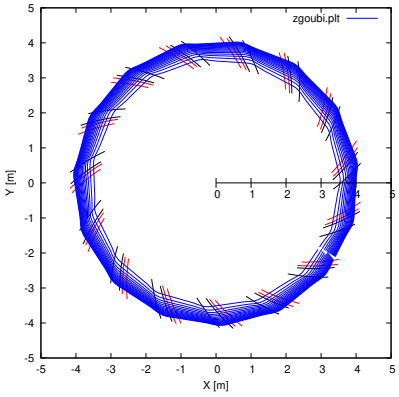

Fig. 10.21 A simulation of a 15-cell proton prototype FFAG ring. The cell is based on a DF spiral sector FFAG dipole doublet. This simulation shows a few closed orbits, at different energies. Red narrow sector: D-dipole; black wider sector: F-dipole

Table 10.3 Design parameters of a 30 MeV proton prototype spiral FFAG

Kinetic energy	MeV	3 to 30
Rigidity	T m	0.250476 to 0.797743
Reference radius (R_0)	m	4
Number of cells		15
Packing factor (pf)		0.35
Orbit excursion	m	0.6 m
Cell tunes, H; V		0.2126; 0.2160
Ring tunes, H; V		3.19; 3.24
Transition gamma		2.9
Magnet		
Type		spiral sector DF doublet
D, F mag. sector angle (A)	deg	2.4; 4.8
Spiral angle (ζ)	deg	41
Scaling index k		7.237
Field B_D; B_F	T	-0.36; 1

10.15 Field in a Spiral Sector Dipole Doublet

FFAG-SPI is based on Eqs. 10.20, 10.33 to model the field from a spiral sector dipole, including for $\mathcal{F}_i(R,\theta)$ (Eq.10.33) the fringe field model of Sec. 18.5. Using that keyword, together with CONSTY, produce a 2D mid-plane field map of the spiral sector doublet. Give a 3D graph of the field.

10.16 Orbits, Scalloping

It is necessary to find the closed orbits prior to characterizing the focusing properties of the lattice. It further allows computing the momentum dependence of optical functions (exercise 10.18), defining the RF law for acceleration (exercise 10.21), etc.

(a) Compute a scan of the periodic orbits $R(\theta)$ across the cell, for a few proton energies ranging in $3 \leq E \leq 30$ MeV. REBELOTE can be used to loop on the energy (by changing the relative particle rigidity D under OBJET), preceded by FIT to find the periodic orbit at the energy of concern.

Plot these orbits $R(\theta)$, and on a separate graph the field $B(\theta)$ along the orbits. These data can be read from zgoubi.plt, using IL=2 under FFAG-SPI keyword.

Show graphically the homothety-rotation of the orbits by plotting the trajectories in a laboratory coordinate system (as in Fig. 10.21).

(b) Illustrate graphically that the orbit "scalloping", *i.e.*, the maximum value of $|R(\theta) - R|/R$, is small $\forall E$, of the order of percents.

(c) This scan provides the momentum dependence of orbit length $C(p)$ and thus average orbit radius $R(p) = C/2\pi$. Give a graphical comparison to theory (Eq. 10.9).

10.17 Zero-Chromaticity

(a) Compute and plot the momentum dependence of the tunes in the 15-cell ring (Fig. 10.21). Use for that either one of the following two methods to obtain the tune values:

(a.1) from the cell transport matrix,

(a.2) from Fourier analysis of small amplitude motion.

(b) It can be observed that the radial tune is constant with momentum, or equivalently with the orbit radius R, this is expected from the scaling law (Eq. 10.7). However the axial tune is R-dependent. Explain why.

(c) In the field model, introduce a R-dependence of the gap of the form Eq. 10.8: this is equivalent to introducing a R-dependence of the fringe field extent, or equivalently of the field form factor $\mathcal{F}(\theta)$ in Eq. 10.10, proper to change the R-dependence of the axial focusing. Using an optimization ("fitting") procedure, compute the value of κ which minimizes the change of ν_y over the energy interval $10 < E < 125$ MeV.

10.18 Optical Functions

Produce the betatron and dispersion functions through a cell, at 3, 15 and 30 MeV.

10.19 Periodic Stability Domain

Vary the scaling index K_F and K_D of respectively the F and D sector dipoles.

(a) Produce a two-dimensional (ν_R, ν_y) tune scan diagram, covering the motion stability area resulting from varying K_F and K_D.

(b) Produce the corresponding (K_F, K_D) stability limit diagram.

10.20 Bucket height, Synchrotron Tune

Check momentum acceptance and synchrotron tune, Eq. 10.27
(a) in stationary bucket mode, at 15 and 180 MeV,
(b) in accelerating bucket mode.

10.21 Acceleration, Transverse Betatron Damping

(a) Produce a simulation of a $3 \rightarrow 30$ MeV acceleration cycle in the 15-cell ring, single particle.
(b) Show graphically that the transverse betatron oscillations satisfy the R-dependence of Eq. 10.31.

10.2.4 FFAG Acceleration Methods

10.22 Hybrid Acceleration

Produce a simulation of hybrid acceleration in the 35 keV $\rightarrow$ 7 MeV, C^{4+}, FFAG injector addressed in Ref. [21, Slides 17-18]. It is suggested to proceed with staged simulations in the following order:

(a) an 8-cell, k=0.7, radial sector DFD ring. The methods of the exercises in Sec. 10.2.1 can be used to construct the cell,

(b) add acceleration, using a single, 5 kV RF cavity,

(c) add betatron acceleration.

10.23 Bucket Acceleration

Produce a simulation of bucket acceleration of a short-lived muon bunch, from 3.6 to 12.6 GeV, following Ref. [23, pp. 4507-4508]. It is suggested to proceed with staged simulations in the following order:

(a) Set up a 225-cell, k=1390, DFD ring. The methods of the exercises in Sec. 10.2.1 can be used to construct the cell.

(b) Add acceleration, 1.8 GV per turn, using 225 (one per cell), 8 MV, 200 MHz RF cavities, harmonic h=675. Re-produce Figs. 5, 6 of Ref. [23, p. 4508].

10.24 Serpentine Acceleration

Produce a simulation of 0.38 to 1.1 GeV serpentine acceleration, following Refs. [24, slide 7],[25]. It is suggested to proceed with staged simulations in the following order:

(a) Set up a 225-cell, k=1390, DFD ring. The methods of the exercises in Sec. 10.2.1 can be used to construct the cell.

(b) Add acceleration, using a single, 60 MV RF cavity, harmonic h=10. Re-produce Figs. 5, 6 of Ref. [23, p. 4508].

References

1. Kolomensky A. A., et al.: Some questions of the theory of cyclic accelerators. Ed. AN SSR, 1955, p. 7, PTE, No 2, 26 (1956)
2. Symon, K. R. Phys. Rev 100, 1247 (1955) Symon, K.R., et al.: D. W. Kerst, L. W. Jones, L. J. Laslett, and K. M. Terwilliger, Fixed-Field Alternating-Gradient Particle Accelerators. Phys. Rev. 103, 1837 (1956)
3. Ohkawa, T.: Two-beam fixed field alternating gradient accelerator. Rev. Sci. Instrum. 29, 108 (1958)
4. Mori, Y.: Developments of FFAG accelerator. 17th international conference on cyclotrons and their applications 2004, Tokyo (Japan), 18-22 Oct 2004. https://www.osti.gov/etdeweb/biblio/20676358
5. Craddock, M.: The rebirth of the FFAG. CERN Courrier (27 July 2004). https://cerncourier.com/a/the-rebirth-of-the-ffag/
6. Collot, J.: The rise of the FFAG. CERN Courrier (19 August 2008). https://cerncourier.com/a/the-rise-of-the-ffag/
7. Ishi, Y.: Status of KURRI Facility. Proceedings of the FFAG 2016 workshop, Imperial college, London, 2016. https://indico.cern.ch/event/543264/contributions/2295846/attachments/1333675/2005286/FFAG16_LONDON_ishi.pdf
8. Pyeon, C.H., et al.: First injection of spallation neutrons generated by high-energy protons into the Kyoto University critical assembly. J. Nucl. Sci. Technol. 46, 1091 (2009)
9. Haj Tahar, M., Méot, F.: Tune compensation in nearly scaling fixed field alternating gradient accelerators. Physical Review Accelerators and Beams 23, 054003 (2020). https://journals.aps.org/prab/abstract/10.1103/PhysRevAccelBeams.23.054003
10. Méot, F.: A Multiple-Room, Continuous Beam Delivery, Hadron-Therapy Installation. Physics Procedia 66 (2015) 361-369. https://www.sciencedirect.com/science/article/pii/S1875389215001984
11. NuFactJ working group. A feasibility study of a neutrino factory in Japan, Version 1.0 (24 May 2001). ******** This link does not work: need a sketch of scaling ffags inside JPARC ring ******* http://www-prism.kek.jp/nufactj/index.html
12. Cole, F. T.: O Camelot, a Memoir of the MURA Years. Cyclotron Conference, East Lansing, USA, May 13-17, 2001. https://accelconf.web.cern.ch/accelconf/c01/cyc2001/extra/Cole.pdf
13. Tanigaki, M., et al.: Construction of FFAG accelerators in KURRI for ADS study. Proc. EPAC 2004 Accel. Conf. 2676-2678 (2004). http://accelconf.web.cern.ch/accelconf/e04/PAPERS/THPLT078.PDF
14. Planche, T., et al.: Design of a prototype gap shaping spiral dipole for a variable energy proton therapy FFAG. NIMA 604 (2009) 435-442.
15. Aiba, M., et al.: Development of 150-MeV FFAG at KEK. FFAG03 Workshop, KEK, Japan, July 7-12,2003. http://130.246.92.181/FFAG/FFAG03_HP/plenary/mori1.pdf
16. Aiba, M., Méot, F., Determination of KEK 150 MeV FFAG parameters from ray-tracing in TOSCA field maps, CERN-NUFACT-NOTE-140 ; CARE-Note-2004-030-BENE ; CEA-DAPNIA-2004-188 - 2004. http://cds.cern.ch/record/806545/files/note-2004-030-BENE.pdf
17. Antoine, S. et al.: Principle design of a proton therapy, rapid-cycling, variable energy spiral FFAG, NIM A 602 (2009) 293-305.
18. Fourrier, J., Martinache, F., Méot, F., Pasternak, J.: Spiral FFAG lattice design tools,application to 6-D tracking in a proton-therapy class lattice. NIM A 589 (2008) 133-142.
19. Méot, F.: RACCAM: a status including magnet prototyping and magnetic measurements. International conference on FFAGs, Fermilab, 21-25 September 2009. https://indico.fnal.gov/event/2672/session/2/contribution/8/material/slides/
20. Mori, Y., et al.: Multi-beam acceleration in FFAG synchrotron. Proc. PAC 2001 Accel. Conf. 588-590 (2001). http://accelconf.web.cern.ch/AccelConf/p01/PAPERS/ROPA010.PDF